Endogenous LRRK2 and PINK1 function in a convergent neuroprotective ciliogenesis pathway in the brain

Enrico Bagnoli[a,b,1] [ID], Yu-En Lin[b,c,1] [ID], Sophie Burel[a,1], Ebsy Jaimon[b,c] [ID], Odetta Antico[a,b] [ID], Christos Themistokleous[a,b] [ID], Jonas M. Nikoloff[b,c] [ID], Samuel Squires[a], Ilaria Morella[d,e] [ID], Jens O. Watzlawik[f] [ID], Fabienne C. Fiesel[f,g] [ID], Wolfdieter Springer[f,g] [ID], Francesca Tonelli[a,b] [ID], Pawel Lis[a,b] [ID], Simon P. Brooks[h], Stephen B. Dunnett[h], Riccardo Brambilla[d,e], Dario R. Alessi[a,b] [ID], Suzanne R. Pfeffer[b,c] [ID], and Miratul M. K. Muqit[a,b,2] [ID]

Affiliations are included on p. 11.

Mutations in Leucine-rich repeat kinase 2 (LRRK2) and PTEN-induced kinase 1 (PINK1) are associated with familial Parkinson's disease (PD). LRRK2 phosphorylates Rab guanosine triphosphatase (GTPases) within the Switch II domain while PINK1 directly phosphorylates Parkin and ubiquitin (Ub) and indirectly induces phosphorylation of a subset of Rab GTPases. Herein we have crossed LRRK2 [R1441C] mutant knock-in mice with PINK1 knock-out (KO) mice and report that loss of PINK1 does not impact endogenous LRRK2-mediated Rab phosphorylation nor do we see significant effect of mutant LRRK2 on PINK1-mediated Rab and Ub phosphorylation. In addition, we observe that a pool of the Rab-specific, protein phosphatase family member 1H phosphatase, is transcriptionally up-regulated and recruited to damaged mitochondria, independent of PINK1 or LRRK2 activity. Parallel signaling of LRRK2 and PINK1 pathways is supported by assessment of motor behavioral studies that show no evidence of genetic interaction in crossed mouse lines. Previously we showed loss of cilia in LRRK2 R1441C mice and herein we show that PINK1 KO mice exhibit a ciliogenesis defect in striatal cholinergic interneurons and astrocytes that interferes with Hedgehog induction of glial derived-neurotrophic factor transcription. This is not exacerbated in double-mutant LRRK2 and PINK1 mice. Overall, our analysis indicates that LRRK2 activation and/or loss of PINK1 function along parallel pathways to impair ciliogenesis, suggesting a convergent mechanism toward PD. Our data suggest that reversal of defects downstream of ciliogenesis offers a common therapeutic strategy for LRRK2 or PINK1 PD patients, whereas LRRK2 inhibitors that are currently in clinical trials are unlikely to benefit PINK1 PD patients.

LRRK2 | PINK1 | ciliogenesis | phosphorylation | brain

Gain-of-function mutations in Leucine-rich repeat kinase 2 (LRRK2) are associated with autosomal dominant Parkinson's disease (PD) and are frequently found in sporadic PD patients (1–3). LRRK2 encodes a multidomain protein containing both a guanosine triphosphatase (GTPase) [Ras of complex (Roc)-C-terminal of Roc (COR)] domain and a protein kinase domain, together with N-terminal protein-interaction domains, recently shown to bind Rab GTPases at distinct sites that regulate the activation state of LRRK2 at membranes (4–7). Pathogenic missense mutations span all domains but are predominantly located within the kinase (e.g., [Gly2019Ser (G2019S)] or Roc-COR domains (e.g., [Arg1441Cys/Gly/His (R1441C/G/H)]) and lead to elevation of LRRK2 kinase activity (8). LRRK2 phosphorylates a subset of Rab GTPases, including Rab1, Rab3, Rab8, Rab10, Rab12, Rab29, Rab35, and Rab43, at a highly conserved Ser/Thr residue positioned within the Switch II–effector binding domain (e.g., Rab8 Thr72; Rab10 Thr73; and Rab12 Ser106) (9, 10). LRRK2-mediated phosphorylation of Rab proteins stimulates binding to RILPL1/2 and JIP3/4 proteins that regulate downstream processes including ciliogenesis (9, 11, 12) and lysosomal stress responses (13–15). Conversely, the metal-dependent protein phosphatase [PPM] family member 1H (PPM1H) dephosphorylates the Switch II domain-phosphorylated residues of LRRK2-regulated Rabs (16). Structural analysis of PPM1H has revealed a "flap domain" within the catalytic fold that specifies binding to phosphorylated Rab (17). PPM1H is mainly localized at the Golgi with additional pools located in the cytosol and mitochondria (16). It contains an N-terminal amphipathic helix that mediates binding to curved membranes, as found at the Golgi, resulting in enhanced catalytic activity (18). PPM1H has been shown to counteract LRRK2's effects on phenotypes such as primary ciliogenesis (18).

Loss-of-function mutations in PTEN-induced kinase 1 (PINK1) cause autosomal recessive PD (19). PINK1 contains an N-terminal mitochondrial targeting domain and a protein kinase domain, flanked by N-terminal and C-terminal regions that facilitate recruitment of PINK1 to the translocase of outer membrane complex that is required for its activation at sites of mitochondrial damage (20–24). Most pathogenic mutations are

Significance

Parkinson's disease (PD) is an incurable brain disorder characterized by loss of dopamine neurons. Mutations in two genes encoding Leucine-rich repeat kinase 2 (LRRK2) and PTEN-induced kinase 1 (PINK1) lead to PD. Previous analysis of LRRK2 mutant mice models had revealed a defect in the cilia of brain cells with associated decrease in glial-derived neurotrophic factor (GDNF) expression. In this study, our analysis demonstrates that PINK1 and LRRK2 operate in parallel signaling pathway in the brain. Notably, PINK1 knock-out mice display cilia defects and reduced GDNF expression akin to LRRK2 mutant mice, suggesting a convergent mechanism for PD. Our findings indicate that treatments aimed at restoring GDNF signaling in the brain may help distinct genetic forms of PD patients.

located within the kinase domain and disrupt its catalytic activity (25–27). Active PINK1 directly phosphorylates Parkin at a conserved Ser65 residue that lies within its ubiquitin-like domain and an equivalent Ser65 residue on Ub, resulting in activation of Parkin via a feed-forward mechanism, triggering Ub-dependent elimination of damaged mitochondria by autophagy (mitophagy) (28–35). Active PINK1 also indirectly induces the phosphorylation of a subset of Rab GTPases including Rab1, Rab8, and Rab13 at a highly conserved Ser residue located within the RabSF3 effector-binding motif (Rab8 Ser111), distinct from the site modified by LRRK2 (36–38). PINK1-mediated Rab phosphorylation inhibits binding of effector proteins including guanine exchange factor and GTPase activating proteins (GAP) (36–38). We previously reported that PINK1 phosphorylation of Rab8 Ser111 impairs the ability of LRRK2 to phosphorylate Thr72 in vitro, however, whether this occurs in cells under endogenous protein expression conditions has hitherto not been assessed (37).

Previous studies have reported cross-talk between LRRK2 and PINK1 mitophagy signaling. An early report suggested that LRRK2 protein expression is increased in human fibroblasts and induced pluripotent stem cell (iPSC)-derived dopaminergic neurons derived from compound heterozygous deletion mutant or homozygous G309D PINK1 mutant patients (39). A further study showed that PINK1-dependent mitochondrial depolarization-induced mitophagy is impaired in human fibroblasts derived from PD patients harboring the LRRK2 G2019S or R1441C mutations and this could be rescued by LRRK2 genetic knockdown or inhibitor treatment (40). The authors suggested this was mediated by LRRK2-mediated Rab10 phosphorylation that impaired its interaction with the autophagy receptor, Optineurin at mitochondria (40). It has also been reported that PINK1-dependent mitophagy was impaired by hyperactive LRRK2 mutations in cell lines and human patient-derived LRRK2 [G2019S] fibroblasts (41). A more recent study reported that decreased mitochondrial depolarization-induced mitophagy in primary cortical neurons derived from LRRK2 R1441C transgenic rats is associated with a significant decrease in phosphorylated Ub compared to nontransgenic neurons (42). That study also showed a significant decrease in mitochondrial depolarization-induced accumulation of phosphorylated Ub and concomitant mitophagy in human iPSC-derived dopaminergic neurons from human fibroblasts expressing the LRRK2 R1441C mutation, although this was not rescued by the LRRK2 inhibitor, MLi-2 (42). Furthermore, LRRK2 has been implicated in regulation of basal mitophagy and analysis of mitophagy in G2019S mutant mice in vivo revealed higher levels of basal mitophagy that was independent of PINK1 and could also be rescued by LRRK2 inhibitors (43, 44).

In this study, we have assessed whether there is any physiological regulation of endogenous LRRK2 by endogenous PINK1 and vice versa in mouse tissues and mouse embryonic fibroblasts (MEFs). We have generated double-mutant PINK1/LRRK2 mice models to assess the role of PINK1 on basal wild-type LRRK2 and pathogenic mutant [R1441C] activity, and conversely, the impact of LRRK2 hyperactivation on PINK1 basal activity in brain and mitochondrial depolarization-dependent activity in MEFs. Our data indicate that knock-out (KO) of PINK1 does not impact the ability of LRRK2 to phosphorylate its Rab substrates; similarly, we do not observe any significant effect of LRRK2 activity on endogenous PINK1-dependent substrate phosphorylation. However, we report a downstream role for PINK1 in the regulation of cilia and glial-derived neurotrophic factor (GDNF) production in the striatum.

Results

PINK1 KO Does Not Impact Basal LRRK2-Mediated Phosphorylation of Rab12 and Rab10 in Mouse Brain and Peripheral Tissues. To investigate the role of endogenous PINK1 in regulating LRRK2

signaling, we crossed LRRK2 R1441C knock-in mice (45–48) with PINK1 KO mice (49–51) that we have characterized in previous studies (Fig. 1A). Double-mutant LRRK2 [R1441C]/PINK1 KO mice were viable and displayed no overt phenotypes. As a readout for LRRK2 pathway activity, we measured phosphorylation of Rab12 at Ser105 [equivalent phosphorylation site to human phospho-serine (pSer)106] and Rab10 at Thr73, using phospho-specific and total antibodies (14, 45) including a new total Rab12 antibody (A26172, *SI Appendix*, Fig. S1 *A–G*). Immunoblot analysis of subdissected striatal (Fig. 1 *B–F*) and cortical (Fig. 1 *G–K*) brain regions from mice treated with or without the LRRK2 inhibitor, MLi-2, confirmed previous data in whole brain that the LRRK2 [R1441C] mutation enhances LRRK2-mediated Rab12 and Rab10 phosphorylation (Fig. 1 *B, D, G*, and *I*) and decreases LRRK2 Ser935 phosphorylation (Fig. 1 *B, E, G*, and *J*) (14, 48). Furthermore, LRRK2-phosphorylated Rab12 or Rab10, quantified in relation to total Rab protein, was not affected by PINK1 KO (Fig. 1 *B, D, G*, and *I*). As expected, MLi-2 treatment markedly reduced Rab12 and Rab10 phosphorylation, concomitant with a decrease in LRRK2 Ser935 phosphorylation (Fig. 1 *B, E, G*, and *J*). We also did not observe any significant changes in the total levels of LRRK2 or PPM1H in PINK1 KO mice lines (Fig. 1 *B, F, G*, and *K*). Broadly similar results were observed for other brain regions analyzed including olfactory bulb (*SI Appendix*, Fig. S2 *A* and *C–E*); hippocampus (*SI Appendix*, Fig. S2 *B* and *F–H*), midbrain (*SI Appendix*, Fig. S3 *A* and *C–E*), thalamus (*SI Appendix*, Fig. S3 *B* and *F–H*), cerebellum (*SI Appendix*, Fig. S4 *A* and *C–E*), brainstem (*SI Appendix*, Fig. S4 *B* and *F–H*), and spinal cord (*SI Appendix*, Fig. S5 *A–D*).

In parallel experiments, we analyzed LRRK2 signaling in peripheral mouse tissues including lung and spleen (*SI Appendix*, Fig. S6). LRRK2-phosphorylated Rab10 or Rab12, quantified in relation to total Rab protein, were not affected by PINK1 KO in the lung (*SI Appendix*, Fig. S6 *A–C*). Similarly, levels of LRRK2 Ser935 phosphorylation and total PPM1H expression were unchanged between WT or PINK1 KO mice (*SI Appendix*, Fig. S6 *A, D,* and *E*). Furthermore, we observed no impact of PINK1 KO on LRRK2-phosphorylated Rab10 levels in the spleen or on LRRK2 Ser935 phosphorylation (*SI Appendix*, Fig. S6 *F–I*). Total Rab12 levels in the spleen were low, which prevented assessment of LRRK2-phosphorylated Rab12.

Behavioral Motor Analysis of Aged Mice Does Not Indicate Interplay between LRRK2 and PINK1 Pathways In Vivo. Previous analyses of LRRK2 [R1441C] knock-in mice and PINK1 KO mice have not detected an overt Parkinsonian motor phenotype (42–48) although we have recently found decreased striatal dopamine (DA) projections and GDNF Receptor alpha staining in LRRK2 mutant mice models (52). We did not observe any gross difference in weight across all four mouse genotypes of 18 wild-type, LRRK2 [R1441C], PINK1 KO, or the double-mutant LRRK2 [R1441C]/PINK1 KO mice (Fig. 2B and *SI Appendix*, Fig. S7 *G* and *H*). We next quantitatively characterized motor function using three of the most widely used behavioral tests, namely rotarod, balance beam, and gait analysis (53, 54) (Fig. 2A). For rotarod testing, we observed slight reduction in the latency to fall for LRRK2 [R1441C] mice compared with wild-type control mice but this was not significantly altered in double-mutant LRRK2 [R1441C]/PINK1 KO mice (Fig. 2G). For the balance beam, we observed a slight increase in the latency to turn by LRRK2 [R1441C] mice compared with wild-type control mice (Fig. 2F), associated with a slight increase in the number of forelimb and hindlimb slips (*SI Appendix*, Fig. S7 *D–F*), however, similar to rotarod testing, this was not significantly altered in double-mutant LRRK2 [R1441C]/PINK1 KO mice (Fig. 2F and *SI Appendix*, Fig. S7 *D–F*). Interestingly, gait analysis revealed a subtle decrease in stride length of the PINK1 KO mice, probably due to the smaller
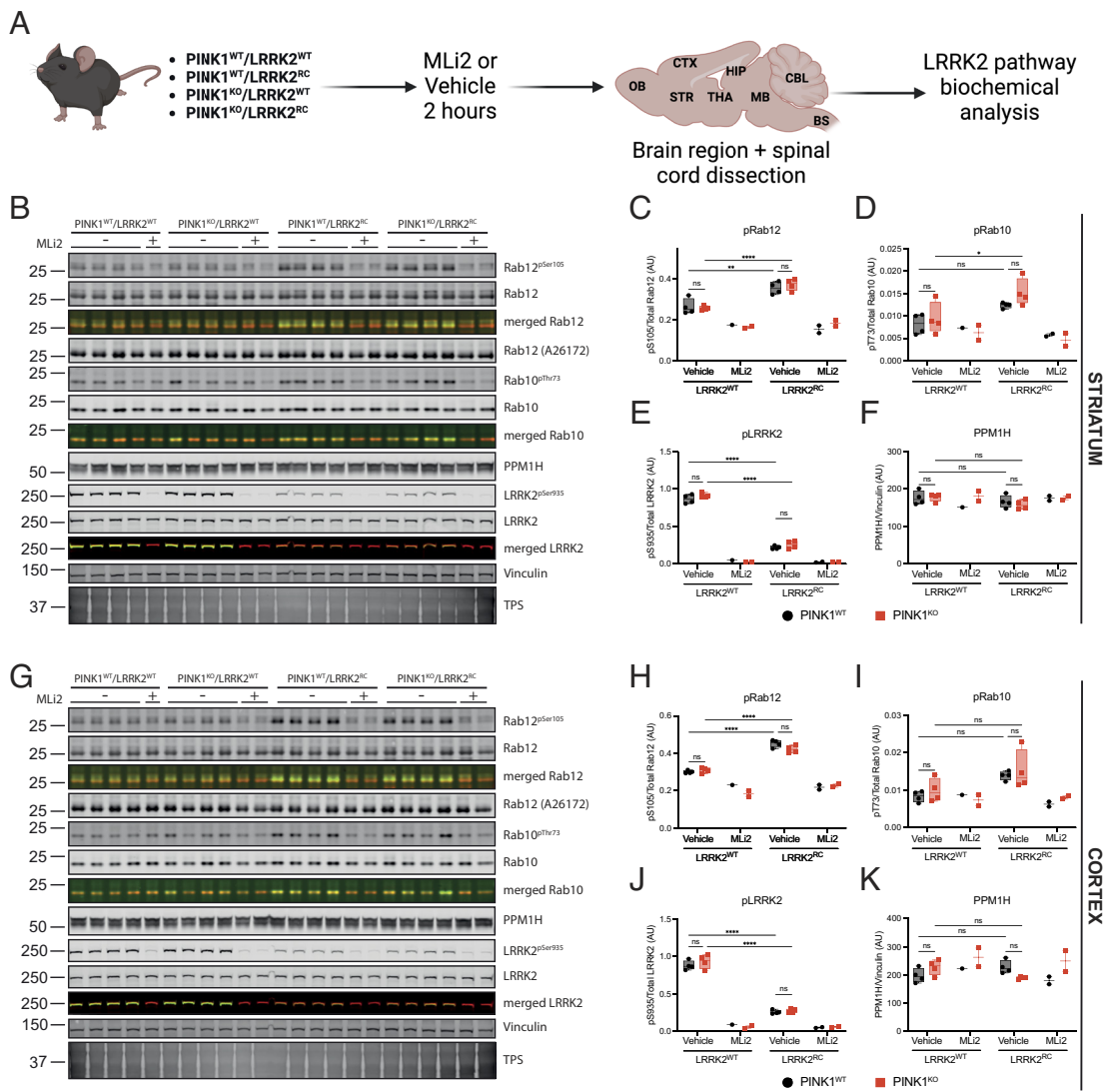
Fig. 1. LRRK2 signaling pathway in the striatum and cortex is not affected by loss of PINK1 in vivo. (*A*) Schematic of methodology followed (*B*) Immunoblot of LRRK2 pathway component in mouse striatum and relative quantification of (*C*) pSer105/total Rab12, (*D*) phospho-threonine73/total Rab10, (*E*) pSer935/total LRRK2, and (*F*) PPM1H/Vinculin. Similarly in (*G–K*) analysis from the mouse cortex. Each lane was loaded with 40 μg of protein lysate from one mouse. In graphs, the black circle represents PINK1^WT while red square PINK1^KO animals. Box and whiskers plot, from min to max with the median line. Ordinary two-way ANOVA with Sidak's multiple comparison test. *$P < 0.05$, **$P < 0.01$, ***$P < 0.001$, ****$P < 0.0001$.

dimension of the mice; however, this was not significantly different in the double-mutant LRRK2 [R1441C]/PINK1 KO mice (Fig. 2*E*). Overall, the motor impairments observed were selective and subtle, and consistent with this we did not observe any impairment for other measures of gait analysis including width of forelimb or hindlimb base (*SI Appendix*, Fig. S7 *A–C*) nor in grip strength (Fig. 2*D*) or proprioception (Fig. 2*C*). Immunohistochemical analysis of brain sections did not reveal any difference in DARPP-32 staining of striatal medium spiny neurons or total striatal volume between mice of different genotypes (*SI Appendix*, Fig. S8 *A–C*). However, analysis of microglia revealed an increase in their number in LRRK2 [R1441C] and PINK1 KO animals, but this was not further exacerbated in the double mutant (Fig. 2 *H* and *I*).

PINK1 Signaling Pathway Is Not Significantly Impacted by Mutant LRRK2 [R1441C]. We next investigated whether mutant LRRK2 impacts endogenous PINK1 signaling in vivo. It has recently been demonstrated that PINK1-dependent, phosphorylated Ub is detectable in mouse tissues, including the brain, under basal conditions, using an enzyme-linked immunosorbent assay (ELISA)-based assay (55). We therefore prepared subdissected brain regions (cortex, midbrain, and cerebellum) and spinal cord from wild-type, LRRK2 [R1441C], PINK1 KO, or the double-mutant LRRK2 [R1441C]/PINK1 KO mice and these were analyzed by an independent laboratory in a blinded manner (*SI Appendix*, Fig. S9). We did not observe any phosphorylated

Ub in samples obtained from the PINK1 KO or double-mutant mice (*SI Appendix*, Fig. S9 *A–D*). Overall we did not observe any significant difference in phosphorylated Ub in select brain regions or spinal cord from LRRK2 [R1441C] mice compared to wild-type littermate control mice (*SI Appendix*, Fig. S9 *A–D*), although interestingly there was a nonsignificant increase in phosphorylated Ub in the midbrain of LRRK2 [R1441C] mice (*SI Appendix*, Fig. S9*B*).

Much of our understanding of PINK1 activation has been obtained under paradigms of mitochondrial damage which cannot be easily recapitulated in vivo (28, 29, 35). We therefore next investigated whether LRRK2 activity influenced PINK1 mediated Ub phosphorylation using immortalized wild-type and homozygous mutant LRRK2 R1441C MEF clones treated with or without oligomycin and antimycin A (O/A) for 24 h to induce mitochondrial depolarization in the presence or absence of PINK1 small interfering RNA (siRNA)-mediated knockdown (Fig. 3). Cells were fully confluent at time of lysis with whole cell extracts analyzed by immunoblotting with anti-LRRK2 antibodies that confirmed uniform expression across all conditions (Fig. 3*A*). Following O/A treatment, we observed robust induction of phosphorylated Ub and the PINK1 dependence was confirmed by loss of signal following siRNA-mediated PINK1 knock-down (Fig. 3 *A* and *B*). Under these conditions we observed a nonsignificant mild increase in phosphorylated Ub between homozygous LRRK2 R1441C mutant MEFs and wild-type controls (Fig. 3 *A* and *B*), in line with the ELISA basal
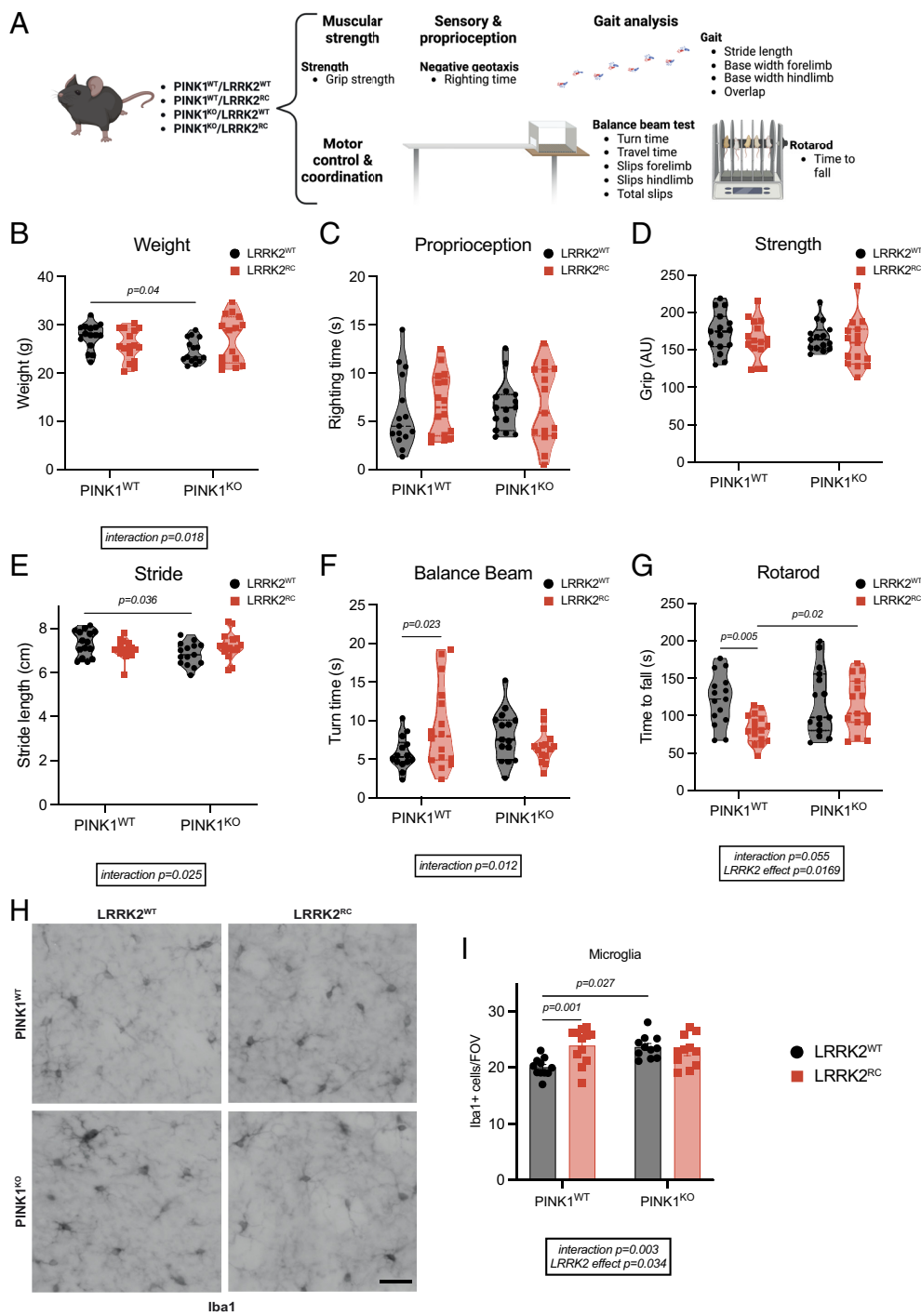
Fig. 2. Behavioral testing in 10.5-mo-old double-mutant PINK1 knockout/LRRK2 R1441C mutant mice does not suggest genetic interaction in vivo. (*A*) A battery of different tests was performed to assess motor function in PINK1 KO and LRRK2 [R1441C] knock-in mice (LRRK2[RC]). (*B*) Weight at 10.5 mo. (*C*) Righting time from negative geotaxis test and (*D*) grip strength. (*E*) Measure of stride length during gait analysis and (*F*) time to turn from balance beam. (*G*) Time to fall from rotarod test. (*H*) Representative images of the microglial marker Iba1 and (*I*) quantification of the Iba1 positive cells. In violin plots, the black circle represents LRRK2[WT] while red squares LRRK2[RC] mice. Ordinary two-way ANOVA with Sidak's multiple comparison test. *$P < 0.05$, **$P < 0.01$, ***$P < 0.001$, ****$P < 0.0001$. N = 15/16 mice per group. (Scale bar, 50 μm.)

midbrain data (*SI Appendix*, Fig. S9*B*). We further observed elevated basal phosphorylation of Rab10 at Thr73 (Fig. 3 *A* and *D*) and Rab12 at Ser105 (Fig. 3 *A* and *E*) in LRRK2 R1441C MEFs compared to wild-type controls and the LRRK2 dependence was confirmed by complete loss of phosphorylation following treatment with the LRRK2 inhibitor MLi-2 (Fig. 3 *A*, *D*, and *E*). We did not observe significant change in Rab 10 or 12 phosphorylation in the LRRK2 R1441C MEFs following O/A treatment in the presence or absence of PINK1 siRNA-mediated knockdown (Fig. 3 *A*, *D*, and *E*) indicating that LRRK2-mediated phosphorylation of Rabs is unaffected under conditions of PINK1 activation and consistent with the in vivo tissue analysis (Fig. 1 and *SI Appendix*, Figs. S2–S6). However, we observed a slight increase in LRRK2 Ser935 phosphorylation and significant decrease in Rab 10 phosphorylation in wild-type MEFs following O/A treatment (Fig. 3 *A* and *D*).

Strikingly, we also observed that PPM1H was up-regulated following O/A treatment in wild-type immortalized MEFs and this was similarly increased in LRRK2 R1441C mutant MEFs. Furthermore, this was not altered by siRNA-mediated knockdown of PINK1 (Fig. 3 *A* and *F*). We next evaluated these changes in primary wild-type MEFs in which cells were grown to 80% confluency prior to lysis and we observed the increase in PPM1H and slight increase in LRRK2 Ser935 phosphorylation following O/A treatment but under these conditions, we did not observe any significant change in Rab10 phosphorylation (*SI Appendix*, Fig. S10 *A–D*).

We next investigated whether LRRK2 activity influences endogenous PINK1-mediated Rab8A Ser111 phosphorylation. We treated independent primary MEF clones derived from wild-type, LRRK2 [R1441C], PINK1 KO, or the double-mutant LRRK2 [R1441C]/PINK1 KO mice, with or without O/A for 24 h to
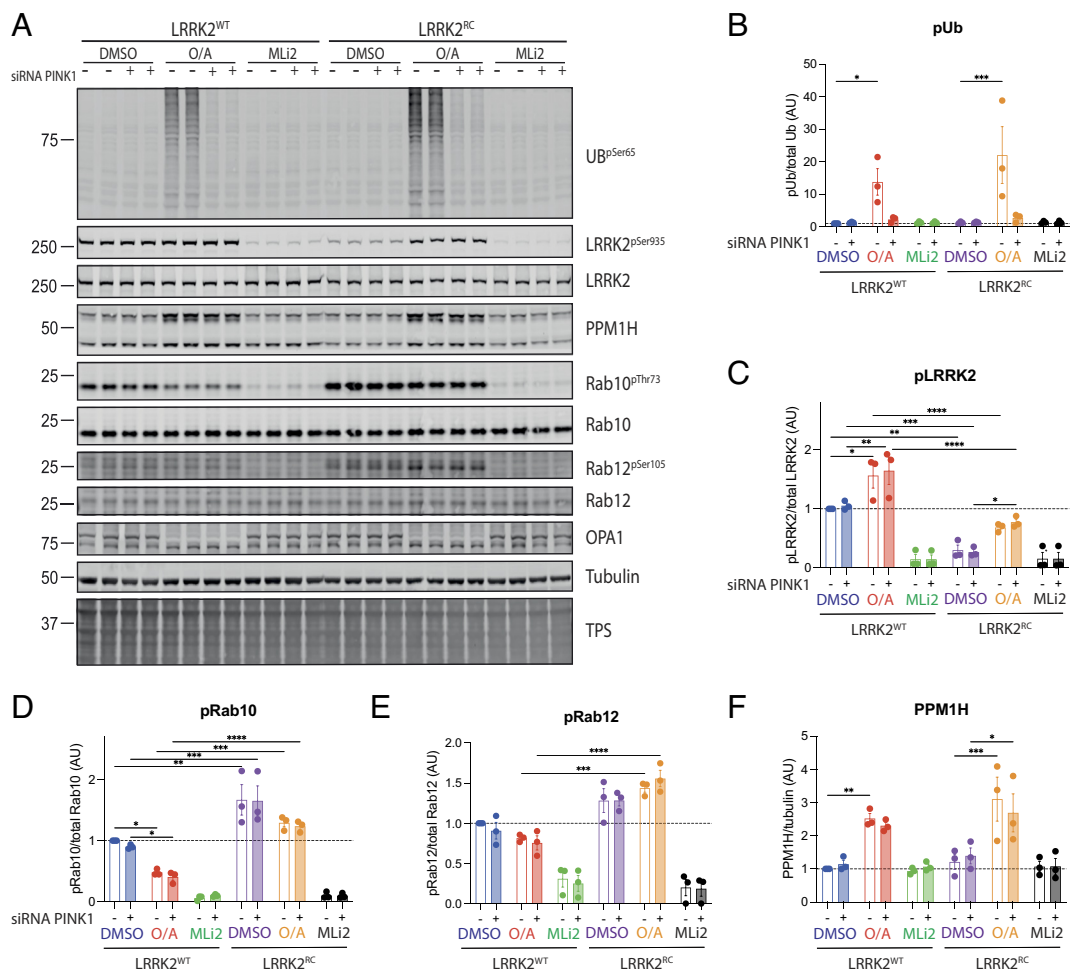
Fig. 3. LRRK2 signaling pathway is not affected by mitochondrial damage-induced activation of PINK1. PINK1 was activated with oligomycin/antimycin for 24 h, while LRRK2 was inhibited by 1 h and 30 min MLi2 treatment. (*A*) Representative immunoblot of PINK1 activation effect on LRRK2 pathway components in LRRK2^{WT} and LRRK2^{RC} MEFs. Quantification from three experimental replicates for pUb, pLRRK2, pRab10, pRab12, and PPM1H is presented in (*B–F*) respectively. Each lane was loaded with 30 μg of protein lysates from one well of a 6-well plate. In graphs, each dot represents one experimental replicate with two biological replicates. − denotes scramble siRNA while +PINK1 siRNA. Bar graphs show mean ± SEM from three independent experiments. Ordinary two-way ANOVA with Sidak's multiple comparison test. *$P < 0.05$, **$P < 0.01$, ***$P < 0.001$, ****$P < 0.0001$.

induce mitochondrial depolarization and with MLi-2 to inhibit LRRK2 kinase activity (100 nM for 1.5 h) (*SI Appendix,* Fig. S11). Cells were grown to 80% confluency and lysed with whole cell extracts analyzed by immunoblotting with anti-LRRK2 and glyceraldehyde 3-phosphate dehydrogenase (GAPDH) antibodies that confirmed uniform expression across all cell types and conditions (*SI Appendix,* Fig. S11*A*). We performed immunoprecipitation-based immunoblotting of total endogenous Rab8A followed by immunoblotting to detect Rab8A phosphorylated at Ser111 or at Thr72; and following O/A treatment, we observed robust induction of Ser111 Rab8A phosphorylation in wild-type MEF clones and observed no difference in both homozygous LRRK2 [R1441C] MEF clones tested (*SI Appendix,* Fig. S11 *A* and *B*). In keeping with the PINK1 dependence of Ser111 Rab8A phosphorylation, we did not observe any signal in PINK1 KO or double-mutant MEF clones (*SI Appendix,* Fig. S11 *A* and *B*). Overall, these results suggest that endogenous PINK1-dependent activation and phosphorylation of Rab8A is not impacted by hyperactivation of endogenous LRRK2 catalytic activity. Consistent with previous analysis we observed basal LRRK2-mediated Thr72 Rab8A phosphorylation in wild-type MEFs and this was increased in homozygous LRRK2 [R1441C] MEF clones but unchanged in either O/A-treated cells or the double-mutant LRRK2 [R1441C]/PINK1 KO MEFs (*SI Appendix,* Fig. S11 *A* and *C*). Similar to previous analysis in primary MEFs, we observed no effect of Rab10 phosphorylation and a slight increase in LRRK2 Ser935 phosphorylation following O/A-treatment, that was independent of PINK1, (*SI Appendix,* Fig. S11*E*). These data further indicate that LRRK2 activity is not affected by basal or mitochondrial-induced activation of PINK1.

PPM1H Is Up-Regulated and Recruited to Mitochondria. To investigate the up-regulation of PPM1H by O/A treatment, we employed previously generated homozygous PPM1H KO immortalized MEFs and corresponding wild-type control immortalized MEF clones (16, 56) and these were treated with O/A for 24 h in the presence or absence of MLi-2. Cells were grown to 80% confluency and lysed with whole cell extracts analyzed by immunoblotting with anti-LRRK2 antibodies that confirmed uniform expression across all conditions (*SI Appendix,* Fig. S12 *A* and *J*). Immunoblotting confirmed PPM1H up-regulation with O/A in wild-type MEFs and the signal was abolished in PPM1H KO MEFs (*SI Appendix,* Fig. S12 *A* and *D*). In the presence of O/A, treatment with MLi-2 abolished phosphorylated Rab10 but did not impact the elevated PPM1H level (*SI Appendix,* Fig. S12 *A* and *G*), pointing to a mechanism independent of LRRK2 kinase activity. Consistent with this, we did not observe any alteration of mitochondrial-stress-induced PPM1H up-regulation in immortalized LRRK2 KO MEFs compared to respective wild-type controls (*SI Appendix,* Fig. S12 *B, E, H,* and *K*). In line with previous siRNA-mediated PINK1 knockdown in MEFs (Fig. 3*A*), we also did not detect any changes in PPM1H up-regulation in immortalized PINK1 KO MEFs compared to wild-type controls (*SI Appendix,* Fig. S12 *C, F, I,* and *L*).

We next performed time course studies of PPM1H protein and messenger RNA (mRNA) expression following O/A treatment in wild-type MEFs by western blot and quantitative RT-PCR, respectively (Fig. 4). This revealed marked time-dependent increase of PPM1H protein evident at 16 h of O/A treatment (Fig. 4 *A* and *B*) associated with slight increase LRRK2 Ser935 phosphorylation (*SI Appendix,* Fig. S13*A*). Under these cell confluency conditions,

we also observed a slight increase in Rab10 phosphorylation with O/A treatment (*SI Appendix*, Fig. S13*A*) that contrasts with maximal confluent culture conditions (Fig. 3 *A* and *D*). Consistent with immunoblotting analysis we observed a significant increase in PPM1H mRNA from 4 h becoming maximal at 16 h using two independent primer pairs (Fig. 4*C* and *SI Appendix*, Fig. S13*C*) and under these conditions we also observed O/A-induced increase in ATF4 mRNA that was maximal at 4 h but sustained to 24 h (*SI Appendix*, Fig. S13*D*) as previously reported (57, 58). To confirm O/A-induced transcriptional up-regulation of PPM1H, we used the transcriptional inhibitor 5,6-dichlorobenzimidazole 1-β-D-ribofuranoside (DRB) and the translational inhibitor cyclohex-imide (CHX) in combination with O/A for 24 h in wild-type and PPM1H KO MEFs (*SI Appendix*, Fig. S13*E*). Consistent with the PPM1H mRNA time course, the O/A-induced increase in PPM1H protein levels was completely prevented when either transcription or translation was blocked (Fig. 4 *D* and *E*). This was confirmed by RT-PCR analysis where the O/A-induced increase in PPM1H mRNA was abolished by transcription inhibition with DRB (Fig. 4*F*). Interestingly, translation inhibition led to a significant increase in basal PPM1H mRNA levels, and this increased further when mitochondria were depolarized following O/A treatment confirmed by two independent primer pairs (Fig. 4*F* and *SI Appendix*, Fig. S13*F*).

To determine the mechanism of PPM1H stabilization, we assessed a panel of agonists, that have previously been reported to disrupt mitochondria by diverse modes of action, in immortalized wild-type MEFs (Fig. 5 *A* and *B*). Under the conditions tested, we found that in addition to O/A, the potassium uniporter, vali-nomycin, that induces mitochondrial depolarization, was able to induce PPM1H stabilization. However, we also observed that multiple compounds were able to induce PPM1H stabilization in the absence of mitochondrial depolarization (as measured by OPA1 cleavage) including the complex I inhibitors rotenone and ivermectin; calcium ionophore ionomycin; pan-AMPK activator MK-8722; and mitochondrial chaperone inhibitor Gamitrinib-

triphenylphosphonium (Fig. 5 *A* and *B*). In future work, it will be interesting to understand better the sensing and signaling mechanism by which PPM1H transcription and protein expression is up-regulated by these mitochondrial perturbations.

PPM1H is predominantly localized at the Golgi with a small pool located at the mitochondria (16, 18). Moreover, our prior analysis demonstrated that artificial localization of PPM1H to mitochondria blocks its ability to act on Thr73-phosphorylated Rab10 (18). We next determined whether PPM1H is being targeted to mitochondria following O/A treatment. Live cell imaging studies of immortalized wild-type MEFs transiently cotransfected with PPM1H-mApple and GFP-mito revealed colocalization on sites of fragmented mitochondria following O/A treatment (Fig. 5 *C* and *D*). Furthermore, this colocalization was readily detected upon 2 min treatment with hypotonic medium that facilitates identification of membrane contact sites (Fig. 5 *C* and *D*). Immunoblotting analysis of mitochondrial fractions of MEFs confirmed basal expression of PPM1H and this increased following O/A treatment (Fig. 5 *E* and *F*).

Mutant PINK1 and LRRK2 Exhibit Convergent Defects in Ciliogenesis in the Brain. We have previously reported that 7-mo-old LRRK2 [R1441C] knock-in mice exhibit significantly fewer primary cilia in cholinergic interneurons within the dorsal striatum compared to wild-type littermate controls (11). We therefore investigated whether endogenous PINK1 plays any role in the mutant LRRK2-mediated cilia defect and analyzed ciliogenesis in dorsal striatal cholinergic interneurons from wild-type, LRRK2 [R1441C], PINK1 KO mice, and double-mutant LRRK2 [R1441C]/PINK1 KO 5-mo-old mice. We observed a small but significant loss of primary cilia in cholinergic interneurons of PINK1 KO mice, of a magnitude less than that seen in LRRK2 [R1441C] mice (Fig. 6 *A* and *C*). Furthermore, we did not observe any exacerbation of the cilia loss in the double-mutant LRRK2 [R1441C]/PINK1 KO mice, suggesting that the regulation of cilia by mutant LRRK2 and PINK1 occurs via parallel pathways (Fig. 6 *A* and *C*). We
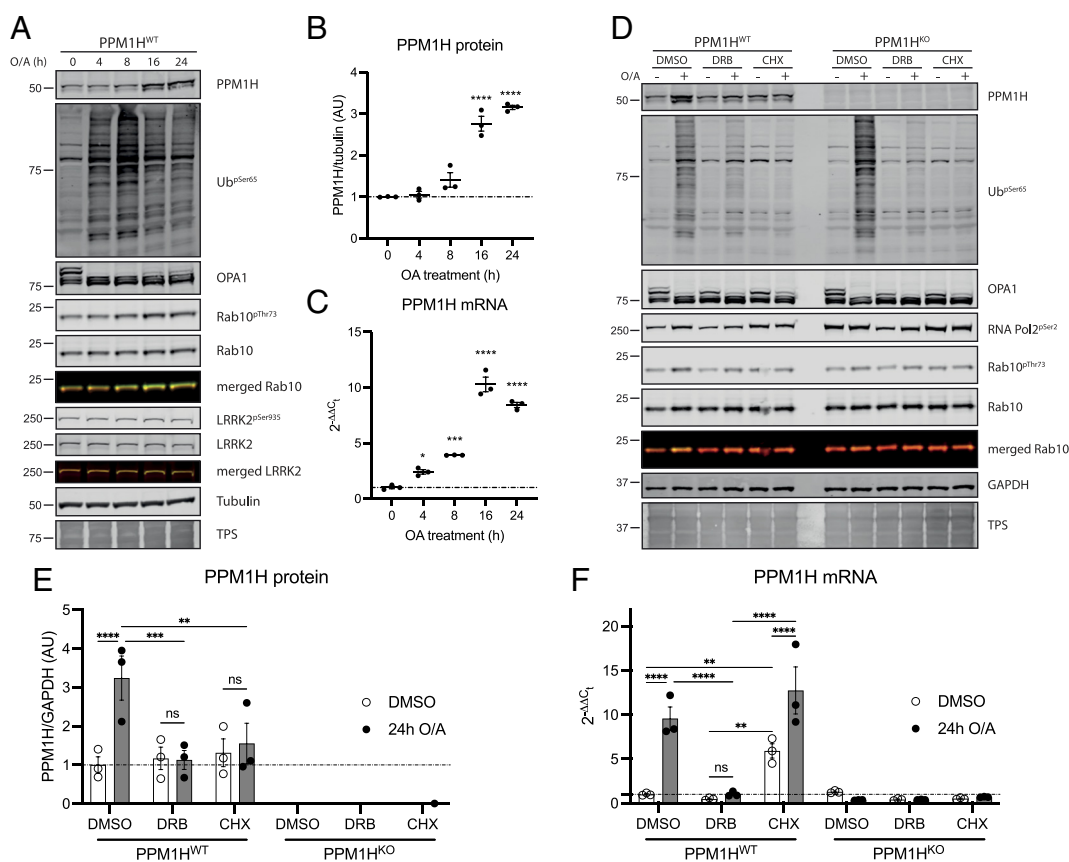

Fig. 4. Endogenous PPM1H is up-regulated following mitochondrial depolarization by a transcriptional mechanism. (*A*) Representative immunoblot from PPM1H^{WT} MEFs treated with oligomycin/antimycin A for 0, 4, 8, 16, and 24 h. (*B*) Quantification of PPM1H protein and (*C*) PPM1H mRNA from three independent experiments. (*D*) Representative immunoblot from PPM1H^{WT} and PPM1H^{KO} MEFs upon 24 h treatment with O/A, O/A + DRB, or O/A + CHX. (*E*) Quantification of PPM1H protein and (*F*) PPM1H mRNA from three independent experiments. Each lane was loaded with 40 μg of protein lysates. Graphs show mean ± SEM from three independent experiments. For *B* and *C*, ordinary one-way ANOVA with Dunnett's multiple comparison test. For *E* and *F*, ordinary two-way ANOVA with Tukey's multiple comparison test from three independent experiments. Empty circles denote dimethyl sulfoxide (DMSO) control while black circles represent O/A treated samples.
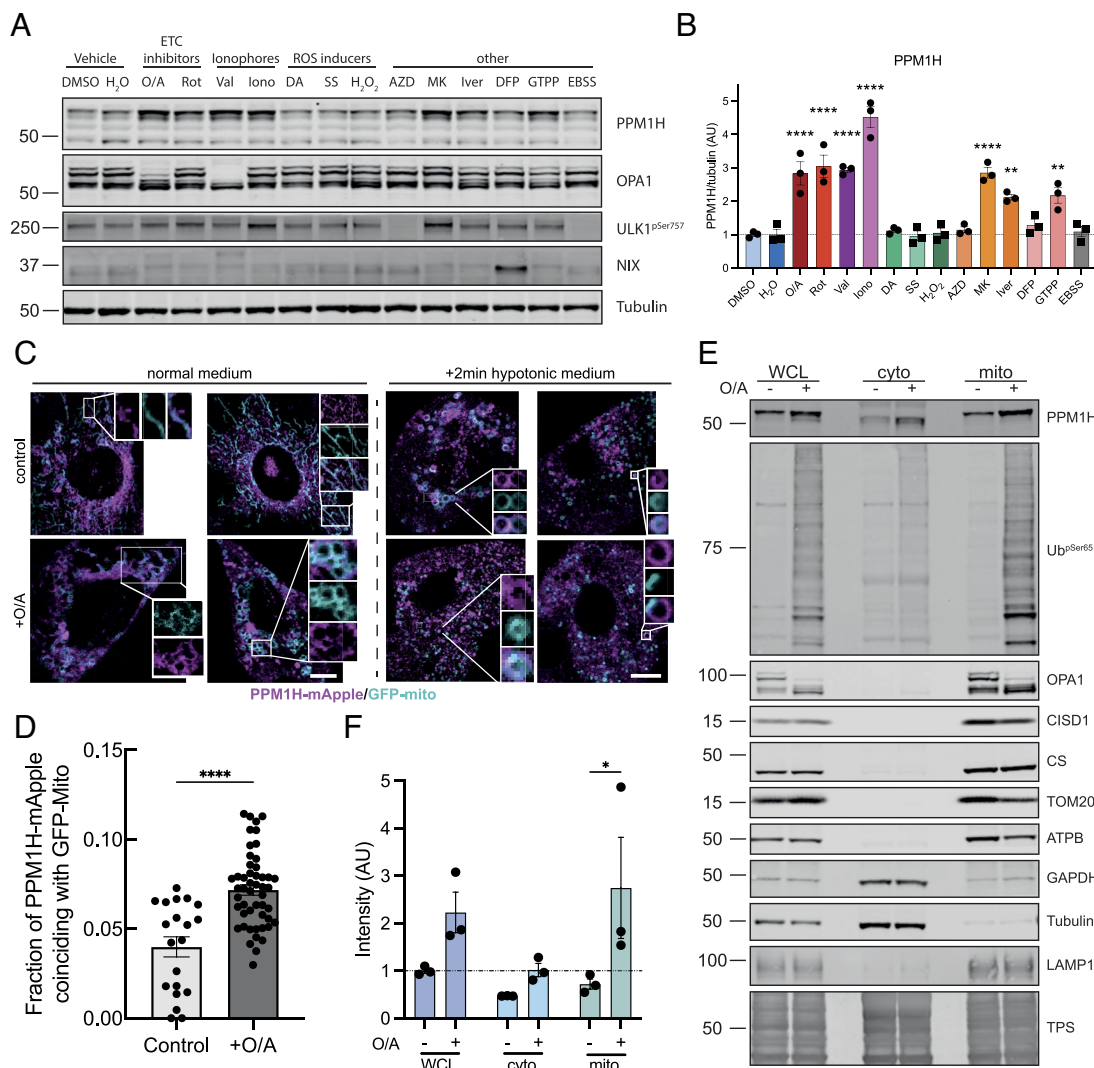
Downloaded from https://www.pnas.org by CARDIFF UNIVERSITY; PERIODICALS ACQUISITIONS on February 4, 2025 from IP address 131.251.0.187.

Fig. 5. Endogenous PPM1H is up-regulated by different mitochondrial stressors and recruited to the organelle. (*A*) Representative immunoblot from PPM1H[WT] MEFs treated with different mitochondrial and cell stressors for 24 h and (*B*) quantification of PPM1H/tubulin from N = 3 independent experiment. (*C*) Live cell imaging of PPM1H-mApple MEF expressing a GFP mitochondrial tag treated with or without oligomycin/antimycin either in normal medium (*Left*) or hypotonic buffer (*Right*) and (*D*) relative quantification of colocalization of PPM1H-mApple and GFP-mito. (*E*) Immunoblot analysis of whole cell extract, cytoplasmic fraction, and crude mitochondrial fraction in PPM1H[WT] MEF after mitochondrial depolarization and (*F*) quantification of PPM1H levels in each of the three cellular compartments. O/A: Oligomycin/Antimycin (1/10 μM) Rot: Rotenone (0. 5 μM); Val: Valinomycin (2 μM); Iono: Ionomycin (5 μM); DA: Dopamine (10 μM); SS: Sodium selenite (7 μM); H$_2$O$_2$: Hydrogen peroxide (50 μM); AZD: AZD8055 (1 μM); MK: MK8722 (10 μM); Iver: Ivermectin (15 μM); DFP: deferiprone (1 mM); GTPP: Gamitrinib-triphenylphosphonium (5 μM); EBSS: Earle's balanced salt solution. Each lane was loaded with 20 μg (15 μg for mitochondrial fraction) of protein lysates. Graphs show mean ± SEM from three independent experiments. For *B–D*, ordinary one-way ANOVA with Dunnett's multiple comparison test versus DMSO (all compounds, black circles and *) or H$_2$O (SS, H$_2$O$_2$, DFP, and EBSS, black squares and #). For *D*, unpaired Mann–Whitney test and for *F*, ordinary two-way ANOVA with Sidak's multiple comparison test from three independent experiments (normalized to whole cell DMSO control). (Scale bar, 50 μm.)

next investigated ciliogenesis in striatal astrocytes where we have previously reported a ciliation defect in LRRK2 mutant models (56) and observed marked loss of cilia in astrocytes of PINK1 KO and LRRK2 [R1441C] mice (Fig. 6 *B* and *E*) but again this was not worsened in the double-mutant LRRK2 [R1441C]/PINK1 KO mice, suggesting that mutant LRRK2 and PINK1 exert parallel and convergent defects on cilia (Fig. 6 *B* and *E*).

Cilia shortening decreases ciliary signaling capacity. We found that PINK1 KO decreased cilia length 30% and this was not exacerbated by the additional presence of the LRRK2 [R1441C] mutation (Fig. 6 *D* and *F*). We have shown that cilia are critical for Hedgehog signaling and production of GDNF by striatal cholinergic interneurons, providing neuroprotection for tyrosine hydroxylase-positive DA neurons (52). In LRRK2 pathway mutant striatum, loss of cilia correlates with loss of Hedgehog-responsive gene expression, leading to decreased expression of Patched (PTCH1) and GDNF RNAs (52). We therefore explored whether cilia loss influenced overall GDNF production. As shown in Fig. 6*H*, LRRK2 [R1441C] striatal cholinergic neurons showed a fivefold decrease in GDNF RNA levels, as monitored by RNAscope fluorescence in situ hybridization (FISH) (Fig. 6*G*). PINK1 KO cholinergic neurons showed a twofold decrease in GDNF expression, in either a wild type or LRRK2 [R1441C] background. When the data were further parsed according to ciliation status (Fig. 6 *G*

and *I*), GDNF expression correlated with the presence of a primary cilium in wild type cells; however, even ciliated LRRK2 mutant neurons were defective in GDNF production. Ciliated PINK1 KO cells showed higher GDNF expression than unciliated PINK1 KO cells but again, even ciliated PINK1 KO cholinergic neurons displayed much less than wild type levels of GDNF expression. These findings are likely explained by the shorter cilia detected in these cholinergic neurons (Fig. 6*D*). These data demonstrate that PINK1 KO influences cholinergic ciliation and GDNF expression in the mouse dorsal striatum. Further work will be needed to explain why the PINK1 KO phenotype is not made more severe when combined with the LRRK2 [R1441C] mutation.

Discussion

Previous studies have established that LRRK2 lies within an endolysosomal signaling network with other PD gene-encoded proteins including VPS35, RAB29, and RAB32 that act upstream of LRRK2 and in which disease-associated mutations lead to LRRK2 hyperactivation and increased Rab phosphorylation (14, 46, 59, 60). Pathogenic activation of LRRK2 exerts downstream effects including lysosomal stress that confers cross-talk with additional PD-linked proteins including VPS13C and GBA1 (14, 61, 62), and this is associated with loss of primary cilia in selective cell types
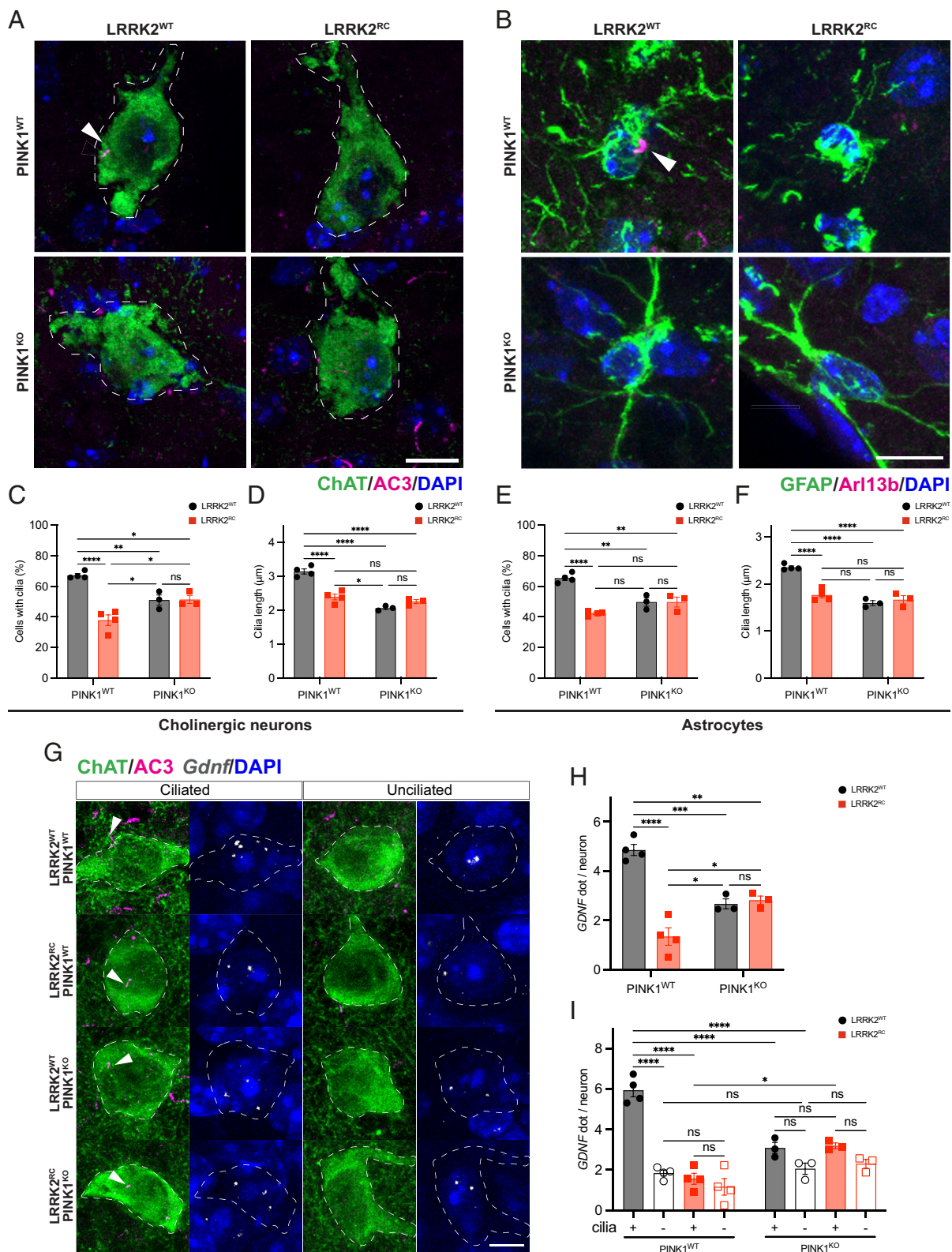
Fig. 6. Loss of PINK1 decreases ciliary signaling in mouse striatum in vivo. (*A* and *B*) Confocal images of sections of dorsal striatum from 5-mo-old WT, LRRK2^{RC}, PINK1^{KO}, and LRRK2^{RC}/PINK1^{KO} mouse brains. (*A*) Cholinergic interneurons were labeled using anti-choline acetyltransferase (ChAT) antibody (green), primary cilia were labeled using anti-AC3 antibody (magenta, white arrow), and nuclei were stained with DAPI (blue). (*B*) Astrocytes were labeled using anti-glial fibrillary acidic protein antibody (green), primary cilia were labeled using anti-ADP ribosylation factor like GTPase 13B antibody (magenta, white arrow) and nuclei were labeled using DAPI (blue). (*C*) Quantitation of the percentage of ChAT$^+$ neurons containing a cilium and (*D*) their cilia length. Similar analyses for astrocytes are shown in (*E* and *F*). (*G*) Confocal images to identify ChAT$^+$ neurons and their cilia as in *A* (*Left* columns) coupled with RNAscope in situ hybridization to detect GDNF transcripts (*Right* columns), segregated by ciliation status in WT, LRRK2^{RC}, PINK1^{KO}, and LRRK2^{RC}/PINK1^{KO} mouse brains as indicated. (*H*) Quantitation of GDNF RNA dots per neuron or (*I*) segregated as a function of ciliation status. Error bars represent SEM from N = 3, 4 mouse brains, with >30 ChAT$^+$ neurons and 25 astrocytes scored per brain. In bar charts, the black circle represents LRRK2^{WT} while red squares LRRK2^{RC} mice. Ordinary two-way ANOVA with Sidak's multiple comparison test. *$P < 0.05$, **$P < 0.01$, ***$P < 0.001$, ****$P < 0.0001$. (Scale bar, 10 μm.)

in the striatum of LRRK2 mutant mice (11, 56). Endo-lysosomal pathways lie downstream of mitophagy and as outlined in the introduction there has been substantial interest in whether the LRRK2 pathway may interplay with the PINK1 pathway. While our results show that knockout of endogenous PINK1 has no significant impact on endogenous LRRK2 activity in vivo, we observed striking ciliary defects and reduced GDNF signaling in the striatum of PINK1 KO mice brain that supports a convergent mechanism.

Based on in vitro studies of recombinant purified Rab8A protein, we had previously reported that PINK1-dependent phosphorylation of Ser111 at Rab8A leads to inhibition of LRRK2-mediated phosphorylation of Rab8A at Thr72 (37). However, we were unable to confirm this interplay in primary MEFs under conditions of endogenous expression levels of Rab8A, PINK1, and LRRK2 (*SI Appendix,* Fig. S9). This suggests that PINK1 and LRRK2 target different pools of Rab8A in cells, consistent with emerging data for their distinct localizations with LRRK2 recruitment to damaged lysosomes (or pericentriolar membranes) by Rab proteins, leading to enhanced phosphorylation of Rab8A (and Rab10) whereas PINK1 is recruited to sites of damaged mitochondria (28, 29, 35). Compelling data for a role of LRRK2 on mitochondrial biology and thereby potential interplay with PINK1 are the demonstration that LRRK2 knockout mice have elevated basal mitophagy while LRRK2 [G2109S] knock-in mice have reduced mitophagy that can be rescued by LRRK2 inhibitors, in distinct central nervous system (CNS) cell types such as dopaminergic neurons (43, 44). Further, Holzbaur demonstrated, in iPSC-derived neurons, that hyperactive LRRK2 mutations or PPM1H KO led to recruitment of the motor adaptor JIP4 to the autophagosomal membrane leading to abnormal activation of kinesin and disrupted transport that would inhibit axonal autophagy (63, 64). Therefore, we cannot rule out interplay of the LRRK2 and PINK1 pathways in specific CNS cell types such as dopaminergic neurons. Furthermore, we cannot rule out that phosphorylation of alternate Rabs by LRRK2, not tested here, may be affected by PINK1. In future work, it will be interesting to undertake a systematic analysis of Rab phosphorylation using unbiased proteomics approaches in select CNS cell types (48).

While the LRRK2 [R1441C]/PINK1 KO double mutant did not show any worsening of motor phenotypes, both the LRRK2 [R1441C] knock-in mice and PINK1 KO mice do not exhibit strong motor defects consistent with previous studies that may also explain the lack of interaction at the behavioral level (Fig. 2). LRRK2 [R1441C] knock-in mice have been reported to be more susceptible to mitochondrial dysfunction (65). Ultrastructural studies of mitochondria at the striatal presynaptic terminals of aged LRRK2 [R1441C] mice are reported to be abnormal with disrupted cristae, and this is associated with reduced ATP production (65). Interestingly, analysis of synaptic function in PINK1 KO and LRRK2 KO rats found age-dependent abnormalities in basal DA for both models and furthermore aged PINK1 rats showed significant disruption of neurotransmitter release with age-dependent increase in potassium evoked striatal DA release which was not observed in LRRK2 KO rats (66). PINK1 KO mice have also been reported to exhibit abnormalities in neurotransmitter release (67) and in future work it would be interesting to determine whether there was any interplay between PINK1 and mutant LRRK2 in these synaptic defects.

Cholinergic interneurons are a rare subset of neurons in the striatum that sense and respond to Sonic Hedgehog secreted by dopaminergic neurons; in turn, these cells secrete GDNF to provide trophic support for dopaminergic neurons (68). Previous work has revealed that hyperactive mutants of LRRK2 including R1441C and G2019S lead to loss of primary cilia in cholinergic interneurons and that this can be detected at 10 wk of age (11, 56). Furthermore, loss of the Rab phosphatase, PPM1H, exhibits a similar ciliary defect providing strong genetic evidence for an important role for LRRK2 pathway activity in cilia formation (56). We report that loss of PINK1 can also lead to primary ciliary loss in striatal cholinergic interneurons and astrocytes; however, we did not observe an exacerbation of the ciliary loss in the double-mutant LRRK2 R1441C/PINK1 KO mice (Fig. 5). Moreover, loss of PINK1 also led to ciliary shortening, the consequence of which led to significantly decreased Hedgehog signaling and decreased GDNF RNA production. These findings imply parallel routes to a convergent pathway between LRRK2 mutations and PINK1 knockout, both triggering loss of neuroprotection in the dorsal striatum by independent routes.

The mechanism of how the PINK1 pathway impacts on cilia is unclear. It was recently reported that human iPSC-derived neuronal precursor cells PINK1 KO mice striatal neurons exhibit shortened primary cilia defects (69). Furthermore, it has been reported that mitochondrial stress, that can be induced by inhibitors of mitochondrial respiration chain complexes, can stimulate ciliogenesis in a variety of CNS cell types mediated via reactive oxygen species (70). It has also been reported that mitochondrial DNA loss in astrocytes lacking the Twinkle helicase exhibit abnormal, elongated, and more motile cilia associated with mitochondrial respiratory chain deficiency and aberrant transcription (71). In future work, it will be interesting to investigate the mechanism of cilia regulation by PINK1.

In prior work, we found that endogenous PPM1H levels were increased in mitochondria of primary mouse cortical neurons following mitochondrial depolarization induced by O/A treatment (51). By immunoblotting, we observed an increase in PPM1H levels in MEF whole cell extracts following O/A treatment and subcellular fractionation and live cell imaging studies revealed higher recruitment of PPM1H to the mitochondrial membrane following O/A treatment. Furthermore, the PPM1H response to mitochondrial depolarization was independent of PINK1 and LRRK2 catalytic activity. Overexpression studies have previously revealed that PPM1H is localized mainly to the Golgi complex with further pools of PPM1H associated with the mother centriole and mitochondria although PPM1H does not act on mitochondrial Ser111-phosphorylated Rab8 (16, 18). At the Golgi, PPM1H strongly colocalizes with Rab8A, Rab10, and Rab29 but less well with Rab12 and overexpression of PPM1H efficiently dephosphorylates Rab10 but not Rab12 suggesting that its major role is to protect Golgi-associated Rabs from LRRK2 phosphorylation and inactivation (18). Herein, we observed that the increase in PPM1H expression by mitochondrial depolarization was not accompanied by a concomitant reduction in phosphorylated Rab10 and this is in line with a previous study in which artificial tethering of PPM1H to the mitochondria led to impaired ability to dephosphorylate total Rab10 (18). In future studies, it will be interesting to better understand the functional consequence of stress-induced PPM1H recruitment to the mitochondria and whether this is important for mitigating LRRK2-dependent phosphorylation of yet unidentified Rabs at the mitochondrial membrane as part of a protective response. Recently autosomal dominant mutations in Rab32 have been identified as a cause of PD and it has further been shown that Rab32 mutations lead to LRRK2 activation and Rab phosphorylation (60). Previous studies have indicated that Rab32 is located at the mitochondria (72–74) and a recent study has demonstrated that LRRK2 forms a complex with Rab32 and aconitate decarboxylase 1 (IRG1) at the mitochondria that is enhanced by *Salmonella* infection and this complex is critical for delivery of antibacterial aconitase from the mitochondria to *Salmonella* containing vesicles (75). There are common mechanisms by which cells respond to mitochondrial stress and bacterial pathogen infection e.g., clearance of damaged mitochondria by mitophagy or bacteria by xenophagy (76). In future work it would be exciting to investigate the potential role of PPM1H at stressed mitochondria and whether this mitigates mutant Rab32-mediated LRRK2 substrate phosphorylation. Further, it would be interesting to determine whether PPM1H is up-regulated in response to *Salmonella* infection to counteract the protective role of the LRRK2-Rab32-IRG1 complex.

In summary, endogenous LRRK2 and PINK1 function in parallel signaling pathways in vivo, however, mutation of both genes leads to impaired ciliogenesis in the brain suggesting a convergent neurobiological mechanism for PD gene pathways. There is growing interest in delivering GDNF to PD patients as a therapeutic strategy and our findings would suggest that both PINK1 and LRRK2 mutant carriers may benefit from such targeted therapies. In contrast, there are several clinical trials underway for evaluating whether LRRK2 inhibitors or antisense oligonucleotide therapies confer disease-modifying benefits for PD patients (77, 78) and our analysis would suggest that patients harboring PINK1 mutations would not benefit from LRRK2 inhibitors and highlight the need for patient stratification for molecular targeted clinical trials in PD.

Materials and Methods

All antibodies, chemicals and reagents, and mouse strains are listed separately in supplementary key reagents table. Furthermore, extensive information regarding the in vivo studies can be found in the ARRIVE table in *SI Appendix*. All methods used in the study, are provided with a link to a detailed protocol.

Animal Husbandry. Mice were housed in temperature-controlled rooms at 21 °C with 45 to 65% relative humidity, 12 h/12 h light/dark cycle, and ad libitum access to food and water. All mice in this study had automatic watering (0.2 micron sterile filtered) and were fed rodent diet "R&M No.3," 9.5 mm pelleted (irradiated, Special Diets Services, UK). All cages had corn-cob substrate (provided as a nest-pack) and sizzle nest material, additionally environmental enrichment was provided for all animals, with a cardboard tunnel for amalgamated females, single-housed males, and squabbling males. Cages were changed as needed, but all cages were changed on at least a two-weekly cycle while mice were regularly subjected to health and welfare monitoring as standard (twice-daily). All mice in this study were maintained on a C57BL/6J background. Mice of both genders were used in all experiments. All animal studies were approved by the University of Dundee Ethical Review Committee and performed under a U.K. Home Officer project license. Experiments were conducted in accordance with the Animal Scientific Procedures Act (1986) and with the Directive 2010/63/EU of the European Parliament and of the Council on the protection of animals used for scientific purposes (2010, no. 63).

Mice Behavioral and Motor Test. Behavioral tests were conducted on 10.5-mo-old mice. Mice were weighted before the start of behavioral tests to make a comparison between genotypes. A description of the battery of assay is available at 10.17504/protocols.io.yxmvm97n6l3p/v1.

Negative geotaxis was assessed by placing the animal onto a mesh grid (30 × 30 cm). The time taken to rotate through 180° from a head down position was recorded as a measure of proprioception.

Grip strength was measured using a grip meter modified from GSM1054 model (Linton Instrumentation) as previously described (79). In two consecutive trials, the mouse was held by the tail and lowered onto the instrument until it gripped the two bars. The mouse was pulled by the base of the tail until the grip loosened. The applied force at which the mouse released the bars was recorded and averaged across the two trials.

Gait analysis, rotarod, and balance beam were conducted as described in refs. 50 and 79. Briefly, gait analysis was carried out using the footprint test. The animal was placed in a clear Perspex corridor apparatus (65 cm L × 15 cm W) and trained to run toward a dark goal box at the end of the corridor until it could reach the box without encouragement. For testing, a paper strip was placed in the corridor and, to leave footprints, the mouse's paws were painted with nontoxic, water-based paints in two different colors to identify the front paws versus the hind paws. The mouse was allowed to run the entire length of the apparatus and reach the goal box. The stride length, the stride width, and the overlap were measured using four paws print, allowing to average three values for each measurement.

Rotarod was carried out using a commercial Rotarod apparatus (Ugo Basile, model 47600). After five sessions of training conducted over five consecutive days (max 5 min/session), mice were tested in two different trials (accelerating rod from 5 rpm to 44 rpm in each trial). The latency to fall was recorded and averaged across

the two trials. For the balance beam, mice were trained on an elevated bridge (1 m in length, 17% angle of ascent, with 1.5 to 0.5 cm tapers across the width) with a dark house box at the high end. During the first day of training, the mouse was placed in front of the house box and allowed to enter the box. The distance from the house box was progressively increased until the low end of the beam. The mouse was then placed at the low end of the beam, facing away from the house box, and encouraged to turn around and transverse the beam until the house box. The test was carried out in two consecutive trials, conducted 1 h apart, and videotaped to allow analysis. The mouse was placed at the low end of the beam, facing away the house box. The time taken to turn around, transverse the beam, and the number of foot slips were recorded and averaged across the two trials.

MLi-2 Treatment in Mice. To ensure LRRK2-dependent phosphorylation of Rabs, mice were treated with the LRRK2 inhibitor MLi-2. The compound was administered to mice via subcutaneous injection as described (10.17504/protocols.io.bezdjf26). MLi-2 was resuspended in a 40% Hydroxypropyl-β-Cyclodextran (Average Mw ~1,460) solution at 6 mg/mL. It was then administered by subcutaneous injection at 30 mg/kg. The Dundee-synthesized MLi-2 (MTA-free) was used for this experiment. Mice were culled 2 h after the injections, tissue collected, and lysed as outlined above.

Mouse Brain Immunohistochemistry—Fluorescence Analysis. Analysis of primary cilia in the mouse brain striatum was performed as previously described (10.17504/protocols.io.bnwimfce). Mice were anesthetized using a commercial solution of Euthatal, before being perfused with phosphate-buffered saline (PBS) and 4% paraformaldehyde (PFA). The brain was then dissected, fixed overnight in 4% PFA at 4 °C, washed, and left in 30% sucrose for 48 h at 4 °C. Whole brains were subsequently embedded in 22 × 22 × 20 mm molds containing O.C.T. compound and kept at −80 °C until sectioning. Sections of the mouse striatum were then obtained with a cryostat with a cutting thickness of 16 μm. Frozen sections were thawed at RT for 15 min and gently washed (2×) with PBS for 5 min. For antigen retrieval, slides were incubated with 10 mM sodium citrate buffer pH 6.0 (preheated to 95 °C) for 15 min at 95 °C. Sections were permeabilized with 0.1% Triton X-100 in 1× PBS at RT for 15 min. Sections were blocked with 2% fetal bovine serum (FBS) and 1% bovine serum albumin (BSA) in PBS for 2 h at RT and were then incubated overnight at 4 °C with primary antibodies. The following day, sections were incubated with secondary antibodies at RT for 2 h. Donkey highly cross-absorbed H+L secondary antibodies conjugated to Alexa 488 and Alexa 568 were used at a 1:2,000 dilution. Nuclei were stained with 0.1 μg/mL DAPI (Sigma). Stained tissues were overlaid with Fluoromount G and a glass coverslip. All antibody dilutions for tissue staining included 1% DMSO to help antibody penetration. Images were obtained using a Zeiss LSM 900 confocal microscope with a 63× 1.4 oil immersion objective. Image visualizations and analyses were performed using Fiji.

Mouse Brain Immunohistochemistry—Colorimetric Analysis. For Iba1 and DARPP-32 staining, mice were anesthetized with Euthatal and perfused with PBS and PFA 4%. Brains were fixed overnight in 4% PFA at 4 °C, washed, and left in 30% sucrose for 24 h at 4 °C. Brains were sliced into 35 μm-thick slices using a freezing microtome and stored at −20 °C until processing for immunohistochemistry. Free-floating sections were rinsed (3×) with tris-buffered saline (TBS) for 10 min and incubated with quenching solution (3% H_2O_2, 10% Methanol in TBS) for 15 min. Sections were subsequently rinsed (3×) in TBS for 10 min and incubated with blocking solution (5% normal goat serum, TBS-Triton 0.1%) for 1 h at room temperature. Incubation with primary antibodies was performed overnight at 4 °C. The following day, sections were rinsed (3×) with TBS Triton 0.1% for 10 min and incubated with the secondary antibodies for 2 h at room temperature. Sections were subsequently rinsed (3×) in TBS-Triton 0.1% for 10 min and incubated for 2 h at room temperature with avidin–peroxidase complex (ABC kit, PK4000, Vector). 3,3′-diaminobenzidine (Sigma) was applied to the slices to visualize Iba1 and DARPP-32 positive cells. Imaged were obtained using a brightfield microscope (Macro/Micro Imaging System, Leica) under a 40× objective and analyzed using Fiji. A more detailed protocol is available at 10.17504/protocols.io.e6nvw1md2lmk/v1.

FISH. RNAscope FISH was conducted as described herein: (bio-protocol.org/prep1423) (52, 56). The RNAscope Multiplex Fluorescent Detection Kit v2 (#323100, Advanced Cell Diagnostics) was used as per the manufacturer with

RNAscope 3-plex Negative Control Probe (#320871) or probe Mm-Gdnf-C1 (#421951). The Mm-Gdnf-C1 probe was diluted 20× in a buffer containing 6× saline-sodium citrate, 0.2% lithium dodecyl sulfate, and 20% Calbiochem OmniPur Formamide. Fluorescent visualization of the hybridized probes was achieved using Opal 690 (Akoya Biosciences). Brain slices were blocked with 1% BSA and 2% FBS in Tris-buffered saline with 0.1% Triton X-100 for 30 min. They were then incubated overnight at 4 °C with primary antibodies in TBS containing 1% BSA and 1% DMSO. This was followed by treatment with secondary antibodies, diluted in TBS with 1% BSA and 1% DMSO, including 0.1 µg/mL DAPI (Sigma) for 2 h at room temperature. Finally, sections were mounted using Fluoromount G and glass coverslips.

Immunoblotting. Protein lysates were subjected to sodium dodecyl sulfate polyacrylamide gel electrophoresis (SDS–PAGE, 4 to 12% Bis-Tris gel or 12% Tris glycine) and transferred onto nitrocellulose membranes. Membranes were then blocked for 1 h in Tris-buffered saline with 0.1% Tween (TBST) containing 5% (w/v) milk and subsequently probed with the indicated antibodies in TBST containing 5% (w/v) BSA overnight at 4 °C. Detection was performed using appropriate secondary antibodies (1:10,000) and scanned using Li-COR Odyssey CLx imaging system. More details can be found on protocols.io (10.17504/protocols.io.ew-ov14znkvr2/v2). Signal intensity was quantified using the Image Studio Software and normalized versus the unphosphorylated protein or the loading control. The amount of protein loaded in each lane is reported for each blot.

PINK1 siRNA. PINK1 knockdown was performed by siRNA in 6-well plates as extensively described (at DOI: 10.17504/protocols.io.kxygx343zg8j/v1). Briefly, 1,00,000 cells were seeded in each well for both LRRK2^WT and LRRK2^RC MEFs. The following day, cells were either incubated with 25 nM of either mouse PINK1 siRNA or scrambling siRNA (Dharmacon). After 48 h, oligomycin and antimycin were added to the culture medium at a final concentration of 1 µM and 10 µM and incubated for another 24 h. The next day (4 d after cell seeding), the LRRK2 kinase inhibitor MLi-2 was added at a concentration of 100 nM for 1 h and 30 min. Finally, cells were quickly washed and lysed on ice, the protein concentration quantified by Bradford and the lysates subjected to western blotting.

Mitochondrial Fractionation. Mitochondrial fractions were purified following steps 21 to 32 of 10.17504/protocols.io.bxmypk7w. Briefly, two 15 cm² dishes (for each sample) were scraped on ice and collected in hypotonic buffer [20 mM HEPES (pH 7.8), 5 mM potassium chloride, 1.5 mM magnesium chloride, 2 mM dithio-threitol (DTT), 1 mM PMSF, and both protease and phosphatase inhibitor cocktails (Roche)]. Cells were homogenized with 45 strokes of stainless steel dounce homogenizer, then, 2.5× mannitol-sucrose buffer [2.5× MSH; 20 mM HEPES (pH 7.8), 525 mM mannitol, 175 mM sucrose, 5 mM ethylenediaminetetraacetic acid (EDTA), 1 mM phenylmethylsulfonyl fluoride (PMSF), and protease inhibitor cocktail (Roche)] was added to the disrupted cells, and the cell homogenates were clarified by centrifugation (700 g at 4 °C for 10 min) to remove nuclei and cell debris. Supernatants were collected and spun down again at 700 g at 4 °C for 10 min before mitochondria were pelleted at 9,000 g for 10 min. The pellet was then resuspended and washed twice in 1× MSH [20 mM HEPES (pH 7.8), 210 mM mannitol, 70 mM sucrose, 2 mM EDTA, 1 mM PMSF, and protease inhibitor cocktail (Roche)] and centrifuged at 9,000 g for 10 min at 4 °C. Finally, mitochondrial pellets were resuspended in 50 µL of lysis buffer, protein quantified, and lysates interrogated by western blotting.

Live Cell Imaging and Quantification. Intracellular localization of PPM1H was monitored in MEFs stably expressing a fluorescent PPM1H-mApple (Addgene 198473) and a GFP-tagged to monoamine oxidase A (Addgene 229232). Stable lines were created by lentiviral infection as per 10.17504/protocols.io.bp2l61z2z-vqe/v1, cell sorting was performed on a Sony SH800, with mApple and GFP double-positive cells selected and expanded. Cells were then seeded in 8-well glass incubation chambers (5,000 cells/well, Nunc 155409) with 0.2 mL of cultured medium. The following day, culture medium was exchanged for phenol red-free medium, with or without oligomycin and antimycin (4 h) and/or hypotonic buffer consisting of 5% DMEM in sterile H_2O (2 min). The 8-well chamber was then placed onto a heated microscopy stage with CO_2 supply and images were taken using confocal z-sectioning. The fraction of PPM1H on mitochondria was quantified by measuring the fraction of PPM1H-mApple labeled pixels that coincide with GFP-Mito labeled pixels after image segmentation using CellProfiler as detailed in 10.17504/protocols.io.j8nlk8qk6l5r/v1.

RT-PCR. PPM1H mRNA were quantified by RT-PCR as previously described (10.17504/protocols.io.81wgbz7r3gpk/v1). Briefly, 15 cm² dishes were washed twice in Dulbecco's phosphate-buffered saline (DPBS) and cells scraped in 1 mL of DPBS. Each sample was then divided, 2/3 were used for western blots and lysed as previously described. The remaining third was spun down, the supernatant removed, and the cell pellet snap frozen and used for RT-PCR. RNA was extracted using the PureLink™ RNA Mini Kit (ThermoFisher) and following the manufacturer's instructions. Cells were dissociated using 300 µL of lysis buffer and by 10× passages in a 20G needle. Total RNA was then eluted in 50 µL of molecular biology water and stored at −80 °C. Complementary DNA (cDNA) synthesis was achieved using the QuantiTect Reverse Transcription Kit (Qiagen) using 1 µg of RNA as template and following the manufacturer's instructions. The obtained cDNA was diluted 1 in 5 before being used for RT-PCR. Two pairs of primers were used to assess PPM1H, while four housekeeping genes were used for normalization (ACTB, GAPDH, RPL13A, and TBP). In each well of a 384-well plate, 2 µL of cDNA were mixed with 3 µL of PowerUp™ SYBR™ Green Master Mix (ThermoFisher) containing 1 µM of forward and reverse primer. The plate was then placed in a thermocycler, the C_t value extrapolated from the amplification curves and the data analyzed using the $\Delta\Delta C_t$ method.

Statistical Analysis. Data were analyzed and plotted using Prism 10.0.3. Statistical difference, set at $P < 0.05$, was calculated either by ordinary one-way ANOVA or by ordinary two-way ANOVA with the appropriate multiple correction test. For non-normally distributed data, a nonparametric test was used instead. P values ≤ 0.05, 0.01, 0.001, and 0.0001 are represented as *, **, ***, and ****, respectively. Graphs represent mean ± SEM, unless otherwise stated. The details of each statistical test, n numbers, and graph used are reported in the relative figure legends.

Author affiliations: ^aMedical Research Council Protein Phosphorylation and Ubiquitylation Unit, School of Life Sciences, University of Dundee, Dundee DD1 5EH, United Kingdom; ^bAligning Science Across Parkinson's Collaborative Research Network, Chevy Chase, MD 20815; ^cDepartment of Biochemistry, Stanford University School of Medicine, Stanford, CA 94305-5307; ^dDepartment of Biology and Biotechnology "Lazzaro Spallanzani", University of Pavia, Pavia 27100, Italy; ^eNeuroscience and Mental Health Innovation Institute, School of Biosciences, Cardiff University, Cardiff CF10 3AX, Wales, United Kingdom; ^fDepartment of Neuroscience, Mayo Clinic, Jacksonville, FL 32224; ^gNeuroscience PhD Program, Mayo Clinic, Graduate School of Biomedical Sciences, Jacksonville, FL 32224; and ^hThe Brain Repair Group, Division of Neuroscience, School of Biosciences, Cardiff University, Cardiff CF10 3AX, Wales, United Kingdom

1. W. P. Gilks *et al.*, A common LRRK2 mutation in idiopathic Parkinson's disease. *Lancet* **365**, 415–416 (2005).
2. C. Paisan-Ruiz *et al.*, Cloning of the gene containing mutations that cause PARK8-linked Parkinson's disease. *Neuron* **44**, 595–600 (2004).
3. A. Zimprich *et al.*, Mutations in LRRK2 cause autosomal-dominant parkinsonism with pleomorphic pathology. *Neuron* **44**, 601–607 (2004).
4. H. S. Dhekne *et al.*, Genome-wide screen reveals Rab12 GTPase as a critical activator of Parkinson's disease-linked LRRK2 kinase. *Elife* **12**, e87098 (2023).
5. E. G. Vides *et al.*, A feed-forward pathway drives LRRK2 kinase membrane recruitment and activation. *Elife* **11**, e79771 (2022).
6. H. Zhu *et al.*, Rab29-dependent asymmetrical activation of leucine-rich repeat kinase 2. *Science* **382**, 1404–1411 (2023).
7. D. R. Alessi, S. R. Pfeffer, Leucine-rich repeat kinases. *Annu. Rev. Biochem.* **93**, 261–287 (2024).
8. A. F. Kalogeropulou *et al.*, Impact of 100 LRRK2 variants linked to Parkinson's disease on kinase activity and microtubule binding. *Biochem. J.* **479**, 1759–1783 (2022).
9. M. Steger *et al.*, Systematic proteomic analysis of LRRK2-mediated Rab GTPase phosphorylation establishes a connection to ciliogenesis. *Elife* **6**, e31012 (2017).
10. M. Steger *et al.*, Phosphoproteomics reveals that Parkinson's disease kinase LRRK2 regulates a subset of Rab GTPases. *Elife* **5**, e12813 (2016).
11. H. S. Dhekne *et al.*, A pathway for Parkinson's disease LRRK2 kinase to block primary cilia and Sonic hedgehog signaling in the brain. *Elife* **7**, e40202 (2018).
12. Y. Sobu *et al.*, Pathogenic LRRK2 regulates ciliation probability upstream of tau tubulin kinase 2 via Rab10 and RILPL1 proteins. *Proc. Natl. Acad. Sci. U.S.A.* **118**, e2005894118 (2021).
13. D. R. Alessi *et al.*, Retromer-dependent lysosomal stress in Parkinson's disease. *Philos. Trans. R Soc. Lond B Biol. Sci.* **379**, 20220376 (2024).
14. P. Pal *et al.*, Parkinson's VPS35[D620N] mutation induces LRRK2-mediated lysosomal association of RILPL1 and TMEM55B. *Sci. Adv.* **9**, eadj1205 (2023).
15. L. Bonet-Ponce *et al.*, LRRK2 mediates tubulation and vesicle sorting from lysosomes. *Sci. Adv.* **6**, eabb2454 (2020).
16. K. Berndsen *et al.*, PPM1H phosphatase counteracts LRRK2 signaling by selectively dephosphorylating Rab proteins. *Elife* **8**, e50416 (2019).
17. D. Waschbusch *et al.*, Structural basis for the specificity of PPM1H phosphatase for Rab GTPases. *EMBO Rep.* **22**, e52675 (2021).
18. W. M. Yeshaw *et al.*, Localization of PPM1H phosphatase tunes Parkinson's disease-linked LRRK2 kinase-mediated Rab GTPase phosphorylation and ciliogenesis. *Proc. Natl. Acad. Sci. U.S.A.* **120**, e2315171120 (2023).
19. E. M. Valente *et al.*, Hereditary early-onset Parkinson's disease caused by mutations in PINK1. *Science* **304**, 1158–1160 (2004).
20. Z. Y. Gan *et al.*, Activation mechanism of PINK1. *Nature* **602**, 328–335 (2022).
21. S. Rasool *et al.*, Mechanism of PINK1 activation by autophosphorylation and insights into assembly on the TOM complex. *Mol. Cell* **82**, 44–59.e6 (2022).
22. P. Kakade *et al.*, Mapping of a N-terminal alpha-helix domain required for human PINK1 stabilization, Serine228 autophosphorylation and activation in cells. *Open Biol.* **12**, 210264 (2022).
23. M. A. Eldeeb *et al.*, Tom20 gates PINK1 activity and mediates its tethering of the TOM and TIM23 translocases upon mitochondrial stress. *Proc. Natl. Acad. Sci. U.S.A.* **121**, e2313540121 (2024).
24. O. G. Raimi *et al.*, Mechanism of human PINK1 activation at the TOM complex in a reconstituted system. *Sci. Adv.* **10**, eadn7191 (2024).
25. A. Kumar *et al.*, Structure of PINK1 and mechanisms of Parkinson's disease-associated mutations. *Elife* **6**, e29985 (2017).
26. A. F. Schubert *et al.*, Structure of PINK1 in complex with its substrate ubiquitin. *Nature* **552**, 51–56 (2017).
27. H. I. Woodroof *et al.*, Discovery of catalytically active orthologues of the Parkinson's disease kinase PINK1: Analysis of substrate specificity and impact of mutations. *Open Biol.* **1**, 110012 (2011).
28. E. A. Goodall, F. Kraus, J. W. Harper, Mechanisms underlying ubiquitin-driven selective mitochondrial and bacterial autophagy. *Mol. Cell* **82**, 1501–1513 (2022).
29. J. N. S. Vargas *et al.*, The mechanisms and roles of selective autophagy in mammals. *Nat. Rev. Mol. Cell Biol.* **24**, 167–185 (2023).
30. L. A. Kane *et al.*, PINK1 phosphorylates ubiquitin to activate Parkin E3 ubiquitin ligase activity. *J. Cell Biol.* **205**, 143–153 (2014).
31. A. Kazlauskaite *et al.*, Parkin is activated by PINK1-dependent phosphorylation of ubiquitin at Ser65. *Biochem. J.* **460**, 127–139 (2014).
32. C. Kondapalli *et al.*, PINK1 is activated by mitochondrial membrane potential depolarization and stimulates Parkin E3 ligase activity by phosphorylating Serine 65. *Open Biol.* **2**, 120080 (2012).
33. F. Koyano *et al.*, Ubiquitin is phosphorylated by PINK1 to activate parkin. *Nature* **510**, 162–166 (2014).
34. A. Ordureau *et al.*, Quantitative proteomics reveal a feedforward mechanism for mitochondrial PARKIN translocation and ubiquitin chain synthesis. *Mol. Cell* **56**, 360–375 (2014).
35. C. Themistokleous *et al.*, Role of autophagy pathway in Parkinson's disease and related genetic neurological disorders. *J. Mol. Biol.* **435**, 168144 (2023).
36. Y. C. Lai *et al.*, Phosphoproteomic screening identifies Rab GTPases as novel downstream targets of PINK1. *EMBO J.* **34**, 2840–2861 (2015).
37. S. Vieweg *et al.*, PINK1-dependent phosphorylation of Serine111 within the SF3 motif of Rab GTPases impairs effector interactions and LRRK2-mediated phosphorylation at Threonine72. *Biochem. J.* **477**, 1651–1668 (2020).
38. D. Pourjafar-Dehkordi *et al.*, Phosphorylation of Ser111 in Rab8a modulates Rabin8-dependent activation by perturbation of side chain interaction networks. *Biochemistry* **58**, 3546–3554 (2019).
39. G. Azkona *et al.*, LRRK2 expression is deregulated in fibroblasts and neurons from Parkinson patients with mutations in PINK1. *Mol. Neurobiol.* **55**, 506–516 (2018).
40. F. Wauters *et al.*, LRRK2 mutations impair depolarization-induced mitophagy through inhibition of mitochondrial accumulation of RAB10. *Autophagy* **16**, 203–222 (2020).
41. F. Bonello *et al.*, LRRK2 impairs PINK1/Parkin-dependent mitophagy via its kinase activity: Pathologic insights into Parkinson's disease. *Hum. Mol. Genet.* **28**, 1645–1660 (2019).
42. M. G. Williamson *et al.*, Mitochondrial dysfunction and mitophagy defects in LRRK2-R1441C Parkinson's disease models. *Hum. Mol. Genet.* **32**, 2808–2821 (2023).
43. A. Tasegian *et al.*, Impact of Type II LRRK2 inhibitors on signaling and mitophagy. *Biochem. J.* **478**, 3555–3573 (2021).
44. F. Singh *et al.*, Pharmacological rescue of impaired mitophagy in Parkinson's disease-related LRRK2 G2019S knock-in mice. *Elife* **10**, e67604 (2021).
45. P. Lis *et al.*, Development of phospho-specific Rab protein antibodies to monitor in vivo activity of the LRRK2 Parkinson's disease kinase. *Biochem. J.* **475**, 1–22 (2018).
46. R. Mir *et al.*, The Parkinson's disease VPS35[D620N] mutation enhances LRRK2-mediated Rab protein phosphorylation in mouse and human. *Biochem. J.* **475**, 1861–1883 (2018).
47. A. F. Kalogeropulou *et al.*, Endogenous Rab29 does not impact basal or stimulated LRRK2 pathway activity. *Biochem. J.* **477**, 4397–4423 (2020).
48. R. S. Nirujogi *et al.*, Development of a multiplexed targeted mass spectrometry assay for LRRK2-phosphorylated Rabs and Ser910/Ser935 biomarker sites. *Biochem. J.* **478**, 299–326 (2021).
49. T. G. McWilliams *et al.*, Basal mitophagy occurs independently of PINK1 in mouse tissues of high metabolic demand. *Cell Metab.* **27**, 439–449.e5 (2018).
50. T. G. McWilliams *et al.*, Phosphorylation of Parkin at serine 65 is essential for its activation in vivo. *Open Biol.* **8**, 180108 (2018).
51. O. Antico *et al.*, Global ubiquitylation analysis of mitochondria in primary neurons identifies endogenous Parkin targets following activation of PINK1. *Sci. Adv.* **7**, eabj0722 (2021).
52. S. S. Khan *et al.*, Loss of primary cilia and dopaminergic neuroprotection in pathogenic LRRK2-driven and idiopathic Parkinson's disease. *Proc. Natl. Acad. Sci. U.S.A.* **121**, e2402206121 (2024).
53. S. P. Brooks, R. C. Trueman, S. B. Dunnett, Assessment of motor coordination and balance in mice using the Rotarod, elevated bridge, and footprint tests. *Curr. Protoc. Mouse Biol.* **2**, 37–53 (2012).
54. S. P. Brooks, S. B. Dunnett, Tests to assess motor phenotype in mice: A user's guide. *Nat. Rev. Neurosci.* **10**, 519–529 (2009).
55. J. O. Watzlawik *et al.*, Sensitive ELISA-based detection method for the mitophagy marker p-S65-Ub in human cells, autopsy brain, and blood samples. *Autophagy* **17**, 2613–2628 (2021).
56. S. S. Khan *et al.*, Pathogenic LRRK2 control of primary cilia and Hedgehog signaling in neurons and astrocytes of mouse brain. *Elife* **10**, e67900 (2021).
57. E. Fessler *et al.*, A pathway coordinated by DELE1 relays mitochondrial stress to the cytosol. *Nature* **579**, 433–437 (2020).
58. X. Guo *et al.*, Mitochondrial stress is relayed to the cytosol by an OMA1-DELE1-HRI pathway. *Nature* **579**, 427–432 (2020).
59. E. Purlyte *et al.*, Rab29 activation of the Parkinson's disease-associated LRRK2 kinase. *EMBO J.* **37**, 1–18 (2018).
60. E. K. Gustavsson *et al.*, RAB32 Ser71Arg in autosomal dominant Parkinson's disease: Linkage, association, and functional analyses. *Lancet. Neurol.* **23**, 603–614 (2024).
61. D. Ysselstein *et al.*, LRRK2 kinase activity regulates lysosomal glucocerebrosidase in neurons derived from Parkinson's disease patients. *Nat. Commun.* **10**, 5570 (2019).
62. M. Kedariti *et al.*, LRRK2 kinase activity regulates GCase level and enzymatic activity differently depending on cell type in Parkinson's disease. *NPJ Parkinsons Dis.* **8**, 92 (2022).
63. D. Dou *et al.*, Regulatory imbalance between LRRK2 kinase, PPM1H phosphatase, and ARF6 GTPase disrupts the axonal transport of autophagosomes. *Cell Rep.* **42**, 112448 (2023).
64. C. A. Boecker *et al.*, Increased LRRK2 kinase activity alters neuronal autophagy by disrupting the axonal transport of autophagosomes. *Curr. Biol.* **31**, 2140–2154.e6 (2021).
65. H. F. Liu *et al.*, Combined LRRK2 mutation, aging and chronic low dose oral rotenone as a model of Parkinson's disease. *Sci. Rep.* **7**, 40887 (2017).
66. R. B. Creed *et al.*, Basal and evoked neurotransmitter levels in Parkin, DJ-1, PINK1 and LRRK2 knockout rat striatum. *Neuroscience* **409**, 169–179 (2019).
67. T. Kitada *et al.*, Impaired dopamine release and synaptic plasticity in the striatum of PINK1-deficient mice. *Proc. Natl. Acad. Sci. U.S.A.* **104**, 11441–11446 (2007).
68. L. E. Gonzalez-Reyes *et al.*, Sonic hedgehog maintains cellular and neurochemical homeostasis in the adult nigrostriatal circuit. *Neuron* **75**, 306–319 (2012).
69. S. Schmidt *et al.*, Primary cilia and SHH signaling impairments in human and mouse models of Parkinson's disease. *Nat. Commun.* **13**, 4819 (2022).
70. J. E. Bae *et al.*, Primary cilia mediate mitochondrial stress responses to promote dopamine neuron survival in a Parkinson's disease model. *Cell Death Dis.* **10**, 952 (2019).
71. O. Ignatenko *et al.*, Mitochondrial dysfunction compromises ciliary homeostasis in astrocytes. *J. Cell Biol.* **222**, e202203019 (2023).
72. N. M. Alto, J. Soderling, J. D. Scott, Rab32 is an A-kinase anchoring protein and participates in mitochondrial dynamics. *J. Cell Biol.* **158**, 659–668 (2002).
73. M. Bui *et al.*, Rab32 modulates apoptosis onset and mitochondria-associated membrane (MAM) properties. *J. Biol. Chem.* **285**, 31590–31602 (2010).
74. P. L. Chen *et al.*, Vesicular transport mediates the uptake of cytoplasmic proteins into mitochondria in Drosophila melanogaster. *Nat. Commun.* **11**, 2592 (2020).
75. H. Lian *et al.*, Parkinson's disease kinase LRRK2 coordinates a cell-intrinsic itaconate-dependent defence pathway against intracellular Salmonella. *Nat. Microbiol.* **8**, 1880–1895 (2023).
76. F. Randow, R. J. Youle, Self and nonself: How autophagy targets mitochondria and bacteria. *Cell Host Microbe.* **15**, 403–411 (2014).
77. D. Jennings *et al.*, LRRK2 inhibition by BIIB122 in healthy participants and patients with Parkinson's disease. *Mov. Disord* **38**, 386–398 (2023).
78. J. M. Taymans *et al.*, Perspective on the current state of the LRRK2 field. *NPJ Parkinsons Dis.* **9**, 104 (2023).
79. S. B. Dunnett, E. M. Torres, L. E. Annett, A lateralised grip strength test to evaluate unilateral nigrostriatal lesions in rats. *Neurosci. Lett.* **246**, 1–4 (1998).
80. E. Bagnoli, Endogenous LRRK2 and PINK1 function in a convergent neuroprotective ciliogenesis pathway in the brain. 10.5281/zenodo.14535133 2024. Deposited 11 December 2024.
81. E. Bagnoli, Endogenous LRRK2 and PINK1 function in a convergent neuroprotective ciliogenesis pathway in the brain. 10.5281/zenodo.11518850. Deposited 7 June 2024.
82. E. Bagnoli, Endogenous LRRK2 and PINK1 function in a convergent neuroprotective ciliogenesis pathway in the brain. 10.5281/zenodo.11519152. Deposited 7 June 2024.
83. E. Bagnoli, Endogenous LRRK2 and PINK1 function in a convergent neuroprotective ciliogenesis pathway in the brain. 10.5281/zenodo.14014456. Deposited 11 December 2024.